Aerosol-Jet-Printed Donor-Blocking Layer for Organic Photodiodes

Mervin Seiberlich, Noah Strobel, Luis Arturo Ruiz-Preciado, Marta Ruscello, Uli Lemmer, and Gerardo Hernandez-Sosa*

Organic photodiodes (OPDs) are optical sensors combining high performance, lightweight mechanical flexibility, and processability from solution. Their fabrication by industrial printing techniques opens a wide range of innovative applications for emerging fields in sensing and the Internet of Things. They typically consist of printed multilayers with functionalities to absorb light, to extract charges, or to reduce detection noise. However, the printing of such device architecture poses a challenge as the deposition of a material can lead to disruption of film morphology or intermixing of materials if its solvent interacts with the previously deposited layer. This work proposes a process to print multilayers from the same solvent system utilizing the aerosol-jet technique. By fine adjustment of the aerosol properties through the tube temperature (T_{Tube}), the drying time of poly(3-hexylthiophene-2,5-diyl) (P3HT) printed layers is significantly reduced. This allows its deposition onto a P3HT-based bulk-heterojunction (BHJ) without negatively affecting its performance. The additional printed P3HT layer, spatially extends the donor region of the BHJ, providing ideal hole extraction and simultaneous noise reduction by the blocking of injected electrons. This donor blocking layer (DBL) yields a noise reduction of two orders of magnitude in OPDs operated under –2 V reverse bias.

1. Introduction

Light sensing devices play a crucial role in communication, industrial monitoring, environmental analysis, energy management, and healthcare applications.[1–3] Presently, these technologies would benefit from photosensing elements with thin, light-weight, mechanically flexible, and customized form factors to expand their applicability towards future wearable and internet of things technologies.[4–7]

Organic photodiodes (OPDs) are thin-film devices with active layers based on organic semiconductors (OSCs) which have demonstrated high performance comparable to typical inorganic based detectors.[8–10] The synthetic flexibility of OSCs has enabled the fabrication of OPDs that are sensitive to wavelengths ranging from the UV to the NIR and can be fabricated via solution processing.[11–14] Furthermore, OPD material systems and architectures have proven to have broad processing flexibility for the maximization of a particular photodetector functionality (i.e., spectral response, speed, or detectivity). Most recently great research effort has been placed on the development of OPD architectures via industrially relevant printing techniques. This opens an avenue of opportunities for the free-form design and integration of very promising light-sensing applications.[15–21] However, to fully exploit the combined potential of printing with the versatility of OSCs, fabrication procedures have to be developed that simplify the printing process of multilayer device architectures while at the same time improve their performance.[22–24]

OPDs are usually driven under reverse bias to enhance charge extraction. This reverse bias commonly results in charge carriers being injected from the electrodes. The resulting dark current is a source of electrical noise that is detrimental to device sensitivity.[25,26] To counterbalance this problem, additional layers are added to the typical multilayer architecture of the device. Under reverse bias, these electron (EBL) or hole blocking layers (HBL) introduce an energy barrier between the electrodes and the active layer, effectively reducing carrier injection.[25,27–29] Consequently, the device shows lower noise, an improved signal-to-noise ratio as well as decreased power consumption.[8,25] The addition of device layers, however, increases fabrication complexity since the already printed layers must not be dissolved or damaged in the process. The integrity of the

M. Seiberlich, Dr. N. Strobel, L. A. Ruiz-Preciado, Prof. U. Lemmer
Dr. G. Hernandez-Sosa
Light Technology Institute
Karlsruhe Institute of Technology
Engesserstr. 13, Karlsruhe 76131, Germany
E-mail: gerardo.sosa@kit.edu
M. Seiberlich, Dr. N. Strobel, L. A. Ruiz-Preciado, Dr. M. Ruscello,
Dr. G. Hernandez-Sosa
InnovationLab
Speyererstr. 4, Heidelberg 69115, Germany
Prof. U. Lemmer
Institute of Microstructure Technology
Karlsruhe Institute of Technology
Hermann-von-Helmholtz-Platz 1, Eggenstein-Leopoldshafen 76344,
Germany

The ORCID identification number(s) for the author(s) of this article can be found under https://doi.org/10.1002/aelm.202000811.

**ADVANCED
SCIENCE NEWS**
www.advancedsciencenews.com

**ADVANCED
ELECTRONIC
MATERIALS**
www.advelectronicmat.de

layers is of particular importance when it comes to printing on top of the BHJ whose functionality depends on its particular intermixed donor–acceptor morphology.[30,31]

Commonly, cross-linking or orthogonal solvent approaches are employed to enable the deposition of multilayer device architectures.[32–36] These two approaches are powerful but also come with disadvantages. The addition of cross-linking side groups or additives to the material can lower the device performance and the choice of orthogonal solvents is restricted by the solubility of the material systems.[37] To circumvent these challenges, Agostinelli and collaborators fabricated OPDs with sequentially deposited donor–acceptor double layers in order to intermix the materials in a post-processing step via controlled heating.[38] This led to a vertical phase separation which acted as a blocking barrier and effectively reduced the dark current. However, the overall device performance was limited by the limited donor-acceptor intermixing in the BHJ region. To date, only three EBLs have been shown to be printable on top of BHJs for OPD applications.[8] Baierl et al. introduced spray-coated poly(3,4-ethylenedioxythiophene) polystyrene sulfonate (PEDOT:PSS) and Grimoldi et al. inkjet-printed poly[3-(3,5-di-tert-butyl-4-methoxyphenyl)-thiophene] (Poly-PT) as blocking layers using orthogonal solvents.[28,39] Both works demonstrated very low dark currents in the order of tenths of nA without lowering their spectral responsivity (SR). Yet, their applicability to other device architectures is still limited by the boundaries of the orthogonal-solvent approach. More recently, Xiong et al. utilized the transfer-printing method to deposit a poly(3-hexylthiophene-2,5-diyl) (P3HT) EBL on top of the BHJ showing successful noise reduction.[40] This method successfully circumvented the issues with layer dissolution; however, it does not provide the freedom of design digital printing techniques offer.

In this work, we propose a new process for fabricating multilayer OPD architectures by exploiting the unique parameter space of the digital and noncontact aerosol-jet printing (AJP) technique. By heating the sprayed gas-droplet mixture shortly before deposition, we control the solvent content in the droplets to influence the drying speed after layer formation. This allows us to print multilayers from the same solvent system, which would otherwise destroy the underlying layer. We use the proposed process to print an EBL on top of a BHJ, in which the EBL is comprised of the same donor material used in the BHJ. Due to the extended usage of the donor material we refer to this layer as the donor blocking layer (DBL). Our approach allows the annealing of the BHJ prior to the printing of the DBL, ensuring optimal intermixing of the BHJ without affecting the DBL and demonstrating a successful reduction of the dark current. For this, we do not rely on orthogonal solvents or cross-linking which were necessary for previously reported fabrication routes for EBLs.

## 2. Results and Discussion

2.1. Aerosol-Jet Printed DBL

Figure 1a,b shows the device architecture and corresponding energy levels of the fabricated OPD, respectively. Prestructured indium tin oxide (ITO) serves as a transparent electrode and spin-coated ZnO nanoparticles as an HBL. We choose the
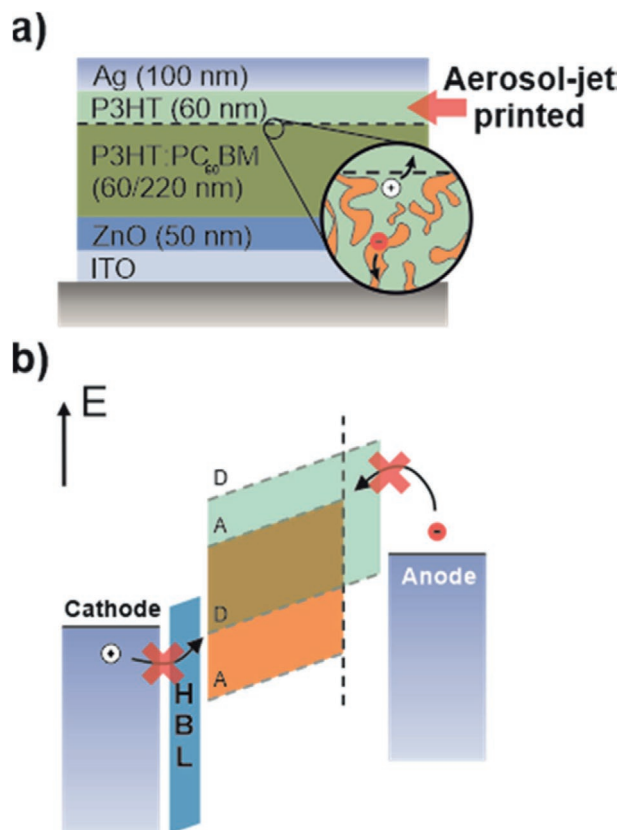
Figure 1. a) Device architecture of the fabricated organic photodiodes. An additional layer of P3HT was aerosol-jet printed on top of the BHJ to serve as an electron blocking layer. b) Energy diagram of the device architecture under reverse bias. The aerosol-jet printed layer spatially extends the donor LUMO of the BHJ hindering electron injection into the acceptor material from the anode.

well-studied blend of the donor P3HT and the acceptor phenyl-C61-butyric acid methyl ester ($PC_{60}BM$) as the photoactive BHJ.[8,41] On top of this active layer, a P3HT DBL is deposited to decrease the electron injection from the anode into the lowest unoccupied molecular orbital (LUMO) of $PC_{60}BM$ due to the higher energetic barrier (see also Figure S1 in the Supporting Information). The DBL deposition is carried out by the digital and contactless AJP technique, which has recently experienced considerable attention in printed electronics research.[8,15,42–45] In this process, the P3HT ink is aerosolized and sprayed onto the BHJ active layer with the help of a focusing stream as depicted in **Figure 2**a. DBL areas are realized by the serpentine printing pattern shown in Figure 2b, which leads to a bottom to top drying front and a higher material deposition at the edges due to the turning points. Notably, the same solvent system is used for the DBL ink as for the BHJ. To prevent damage to the active layer, we tune the effective solvent concentration in the aerosol droplets by adjusting the temperature (T_{Tube}) of the tube which transports the aerosol to the nozzle.

T_{tube} was increased from room temperature to up to 150 °C in order to raise the P3HT concentration in the droplets and to thereby also increase the drying speed of the printed DBL. Figure 2c shows white-light interferometer pictures of the printed P3HT layers on top of the BHJ for various T_{tube}. It can
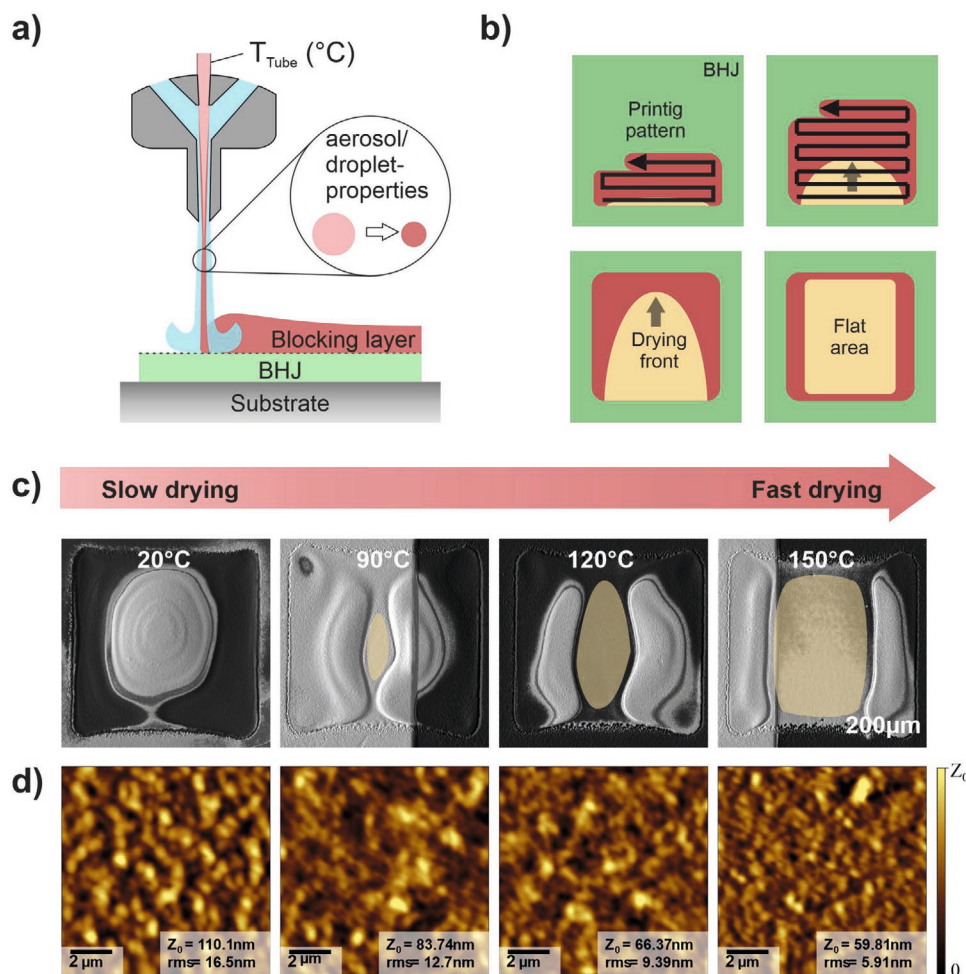
Figure 2. a) Schematic visualization of aerosol-jetting of multilayers with the same solvent base for each layer by adjusting the aerosol properties with the tube temperature T_{Tube}. b) Serpentine printing path and drying front. c) Withe light interferometer pictures of dried P3HT pads on top of a preannealed P3HT:PCBM BHJ. d) AFM pictures of the homogenous areas corresponding to the same printed layers showing smooth and closed layers.

be observed that the sample deposited at room temperature looks inhomogeneous and material flowed towards the center by drying dynamics. At this temperature, due to the high solvent content of the ink and the time needed for its drying, it is expected that the deposited material will intermix with the BHJ and result in an altered OPD performance. We observed that higher T_{Tube} significantly increased drying speed in the center leading to more homogenous printed areas. For $T_{Tube} = 150\ °C$, the area in the center reaches a suitable size and homogeneity for the OPD pixel. Note, the increased material accumulation at the sides of the printed area is not a coffee ring in the classical sense but stems from the chosen serpentine printing path that leads to a higher material deposition at the turning points. Compared to room temperature, we shortened the drying time from minutes down to seconds and consequently reduced the amount of time that the solvent was in contact with the previously deposited BHJ layer. Increasing T_{Tube} over 150 °C reduces the solvent content in the droplets further and eventually surpasses the solubility limit of P3HT. Thus, an aggregation of P3HT occurs and the dry material deposition results in a rough and inhomogeneous layer (see Figure S2 in

the Supporting Information). We want to emphasize that an increased substrate temperature would not lead to the desired result as the solubility of the BHJ materials strongly depends on temperature.[46] Thus a warmer substrate would assist in dissolving the already deposited active layer (see Figure S3 in the Supporting Information). To avoid this, all experiments were performed at a substrate temperature of 20 °C. Figure 2d shows atomic force microscopy (AFM) images of the printed DBLs. The microscale roughness in the center of the printed areas decreases with faster drying times from 16.5 nm at 20 °C to 5.9 nm at 150 °C. A reduced roughness usually favors improved device performance.[47,48] Moreover, no holes are visible, which eliminates the risk of short circuits in the final multilayer device.

2.2. OPD Characterization

To examine the effect of the aerosol-jet printed DBL on the device performance, we compare three kinds of devices. One device with DBL printed at $T_{Tube} = 150\ °C$, representing an optimized quick drying time and one device with DBL printed at

**ADVANCED
SCIENCE NEWS**
www.advancedsciencenews.com

**ADVANCED
ELECTRONIC
MATERIALS**
www.advelectronicmat.de

$T_{Tube} = 20$ °C, representing a very slow drying time. Furthermore, a device fabricated without any additional blocking layer serves as a reference. The two temperatures were chosen as representative extremes, whereas the other printing parameters like gas flow, aerosol density, printing speed, and pattern were kept constant over the different samples. We use a spin-coated BHJ layer of only 60 nm in thickness to show the potential of the proposed technique even for very thin layers.

2.2.1. Current–Voltage Characteristics

The current–voltage characteristics of the different devices in the dark and under illumination are shown in **Figure 3**a–c. Comparing their dark currents under reverse bias, we observe a trend: The reference shows a high dark current of 6880 µA cm^{-2} at −2 V. It is reduced by one order of magnitude by introducing the DBL printed at $T_{Tube} = 20$°C (425 µA cm^{-2}) and even by about two orders of magnitude for $T_{Tube} = 150$ °C (90 µA cm^{-2}). We observed a similar trend for devices with thick BHJ (See Figure S4 in the Supporting Information). This demonstrates the blocking capability of the DBL and highlights the role of T_{tube} on device performance. We correlate the reduced dark current for DBLs printed at higher T_{tube} to their faster drying time resulting in lower damage to the previously deposited BHJ. Printing at $T_{Tube} = 150$ °C prevents an intermixing with the BHJ enabling P3HT to effectively block electron injection into the BHJ. In contrast, the P3HT printed at $T_{Tube} = 20$ °C has a long time to intermix with the BHJ and a full intermixed layer is expected. Therefore, the reduced dark current in this sample more likely stems from the increased layer thickness than from charge carrier blocking. This trend was confirmed by numerical simulations in which we used the same device stacks (material layers and thicknesses) as in our experiments combined with parameters available in literature that closely describe the physical characteristics of our materials (See Figures S5 and S6 in the Supporting Information). [49–51] Compared to literature the absolute dark current is quite high (see Table S1 in the Supporting Information)[8] We attribute this to the thin BHJs used and the fabrication under ambient conditions.[25] Moreover, the blocking capability of the ZnO HBL might be reduced by our encapsulation procedure which includes UV-exposure. This is known to generate photoshunts in solar cells[52] and will require an OPD specific investigation in the future. Nonetheless the effect of the DBL is comparable to other EBLs from literature, as can be seen in the relative change of the dark current and the favorable effect on its rectification.[39,40] Most importantly, the present method increases the material library that could be tested for EBLs in the future without the limit of orthogonal solvents.

Interestingly, under forward bias, the dark current of the reference device is more than two orders of magnitude higher than that of the device with a DBL printed at $T_{Tube} = 150$ °C. This can be explained by the increase in series resistance when adding the DBL. Usually we would not expect an offset between the current–voltage characteristics of the dark and illuminated measurements. This is a hint for photomediated charge injection effects which could be related to trap states in the BHJ or to a reduced injection barrier through the UV exposure.[53–55]
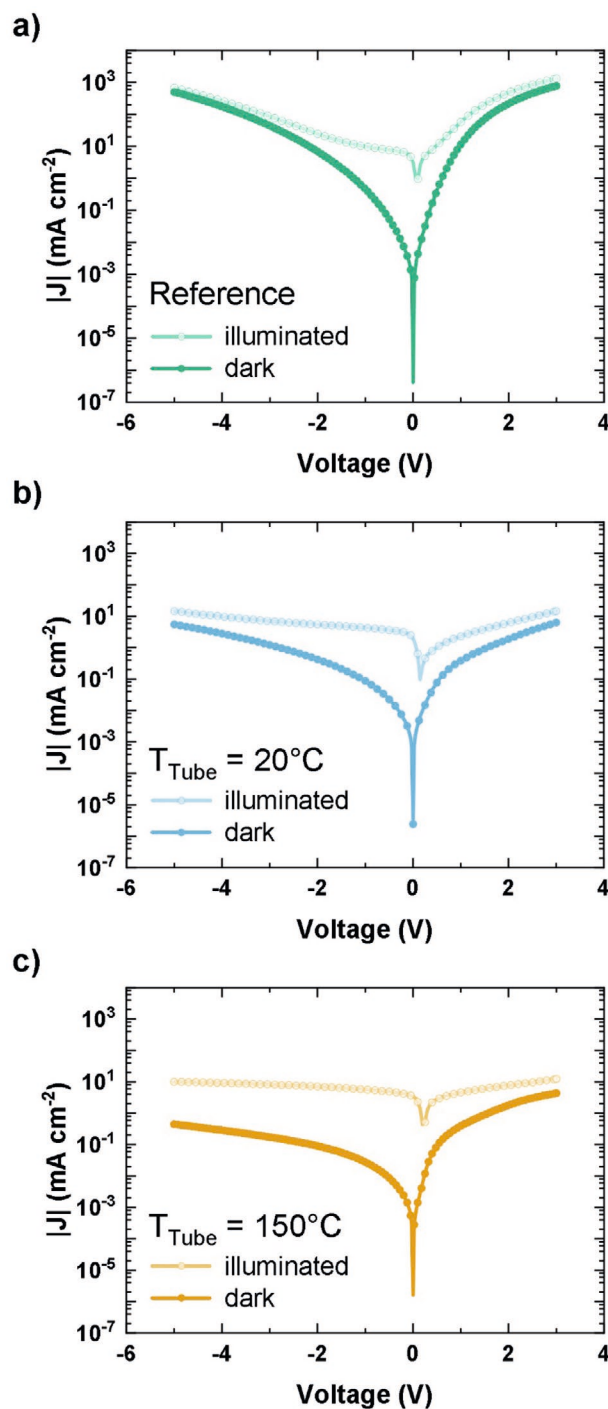
Figure 3. Current–voltage characteristics from −5 to 3 V of illuminated OPDs with a) no DBL b) a DBL printed at 20 °C and c) a DBL printed at 150 °C as well as their respective dark currents, demonstrating different dependencies in the photodiode regime.

However, for OPDs the behavior in the reverse bias regime is more relevant and further investigations are out of scope for this work. Finally, the positive influence of the DBL is also visible in the device currents under illumination (100 mW cm^{-2}) and reverse bias voltages. While the reference seems to be

strongly limited by the dark current for voltages below −2 V, the devices with DBL shows a clear photoresponse over the entire voltage range. This is a direct consequence of the reduction in the field-driven injection of charge carriers.

2.2.2. Spectral Responsivity, Noise, and Detectivity

To determine light-to-current conversion, we measured the SR of the devices (Figure S7, Supporting Information). At −2 V reverse bias, the reference without blocking layers reaches 0.434 AW^{-1}, the highest SR of the three devices. At the same voltage, the device with T_{Tube} = 20 °C exhibits an SR of 0.178 AW^{-1} while the device with T_{Tube} = 150 °C reaches 0.214 AW^{-1}. The reduction of the SR after printing may result from a slight change in the BHJ's morphology or photoconductive gain effects present in the reference device which are reduced by the DBL.[31,55] To bring these values into context and appropriately compare the sensitivity of all three devices we need to first determine the specific detectivity (D^*). This figure of merit relates the device photoresponse to the device noise current. It is defined by the ratio of the SR to the noise spectral density (S_n) and is normalized by the area A of the device as shown in Equation 1.[8,56] In the literature, D^* is commonly written in terms of the dark current by assuming white noise to be dominant. This often leads to an overestimation of the detectivity and should be avoided where possible. For further information about frequency-dependent noise, S_n and D^*, we refer the interested reader to the recent literature.[8,56]

$$D^*(\lambda, f) = \frac{SR(\lambda)\sqrt{A}}{S_n(f)} \quad (1)$$

Figure 4 shows $S_n(f)$ and the resulting frequency-dependent $D^*(f)$ for a −2 V reverse bias at the peak SR (λ = 560 nm). It can be observed that the device fabricated at T_{Tube} = 150 °C shows a D^* more than two orders of magnitude higher than the reference device and one order of magnitude higher compared to the device printed at T_{Tube} = 20 °C. This confirms the functionality of the presented approach by demonstrating that the noise reduction of the devices is related to the faster drying times of

the DBL. The absolute detectivity of about 10^{11} Jones matches the state-of-the-art performance for P3HT:PC$_{60}$BM based OPDs.[8] Furthermore, the D^* of the device fabricated at T_{Tube} = 150 °C shows a frequency-independent range starting around 50 Hz, while for the device with T_{Tube} = 20 °C and the reference device the measured D^* remains frequency dependent (further details regarding the frequency f_{white} that marks the white noise regime can be found in the Supporting Information). This indicates a considerable frequency-dependent 1/f-noise contribution for the reference device and the device printed at T_{Tube} = 20 °C possibly stemming from fluctuations due to charge carrier trapping or recombination.[57] For the devices printed at T_{Tube} = 20 °C, the reduced frequency dependence might be caused by trap states introduced by energetic disorders in the BHJ at the interface to the electrode.[53,58,59] For the DBL printed at T_{Tube} = 150 °C, only pure P3HT is expected to have an interface to the electrode, thus reducing the trap state density. Further studies are in progress to develop a deeper understanding of the precise underlying mechanisms.

The voltage dependence of D^* for different reverse bias is shown in Figure S8 (Supporting Information) and their representative values in **Table 1**. When increasing the reverse bias, we observe a strong decrease in D^* for the reference device and the device printed at T_{Tube} = 20 °C. At first glance, this might seem counterintuitive considering that the SRs becomes larger for higher reverse bias, indicating an improved charge extraction (see Figure S7 in the Supporting Information). However, when we take the noise into account, which increases at a higher rate, this effect is canceled out. In contrast, the device printed at T_{Tube} = 150° shows a slight increase of D^* at −4 V. The same holds for devices with thicker BHJs (see Figure S9 in the Supporting Information). This demonstrates successful noise reduction by the DBL and suggests a minimized negative influence of the printing step on the morphology of the BHJ.

2.2.3. Linear Dynamic Range

Additionally, we characterized the linear dynamic range (LDR) of the devices, which indicates the range of intensities where the OPD current response is linear with the incident optical
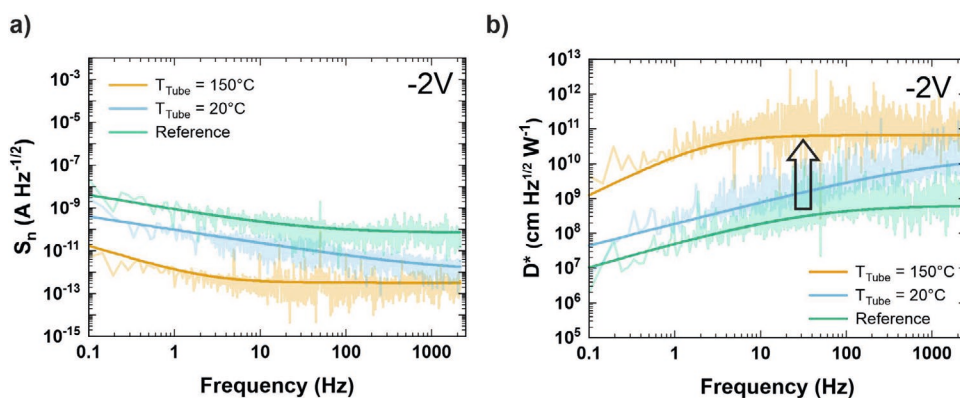
Figure 4. a) Spectral noise density S_n with fitted data and b) calculated specific detectivity D^* measured at −2 V reverse bias. The solid line represents the fitted data (See the Supporting Information for details).

**ADVANCED
SCIENCE NEWS**
www.advancedsciencenews.com

**ADVANCED
ELECTRONIC
MATERIALS**
www.advelectronicmat.de

Table 1. Overview of FOMs at different reverse biases. $D*$ & SR are measured at 560 nm and 173 Hz chopper frequency.

Device	i_{Dark} [mA cm^{-2}]	SR [AW^{-1}]	$D*$ [cm Hz$^{1/2}$W^{-1}]			−3 dB Cut-off [kHz]	LDR [dB]	
	(−2 V)	(−2 V)	(−0 V)	(−2 V)	(−4 V)	(−2 V)	(0 V)	(−2 V)
T_{Tube} 150 °C	0.090	0.214	3.77×10^{10}	6.59×10^{10}	9.15×10^{10}	864	132	>60
T_{Tube} 20 °C	0.425	0.178	2.45×10^{10}	3.77×10^{9}	1.47×10^{9}	457	87	>38
Reference	6.880	0.434	3.75×10^{10}	4.82×10^{8}	1.90×10^{8}	2348	102	>22

power. It is shown in Table 1 for 0 V bias and −2 V reverse bias. The OPD with DBL printed at $T_{Tube} = 150°$ outperforms the other two devices in this respect. It shows an LDR of 132 dB, about 30 dB larger than the LDR of the reference and about 40 dB larger than the LDR of the device printed at $T_{Tube} = 20$ °C. At −2 V bias, the maximum intensity achievable by the light source limited the maximal measuring range (see Figure S10 in the Supporting Information). Therefore, LDRs are most likely underestimated and only give information about the lower limit of the LDR (labeled with ">"). Nonetheless, the low-intensity limit given by the dark current for the device printed at $T_{Tube} = 150$ °C is about 38 dB lower than for the reference device without DBL.

2.2.4. Electrical Bandwidth

Finally, the detection speed of OPDs was quantified by measuring their −3 dB cut-off frequency, B.[8] Representative values can be found in Table 1, and the measurement in Figure S11 in the Supporting Information. The reference device reaches 650 and 2348 kHz at 0 and −2 V, respectively. While the effect of increased speed at reverse bias is less visible in the device with DBLs printed at $T_{Tube} = 150°$, it still reaches 864 kHz at −2 V bias, which is among the fastest OPDs with P3HT:PC$_{60}$BM as an active layer.[8] The device with $T_{Tube} = 20°$, on the other hand, shows a reduced speed of 457 kHz compared to 0 V bias. The higher detection speed of the device printed with the optimized tube temperature is yet another demonstration of the successful DBL deposition and conservation of the beneficial photoactive layer morphology that results in high performance and functionality.

3. Conclusions

Here we present a new process for printing OPD blocking layers without the need for orthogonal solvents or crosslinking, using the noncontact and digital aerosol-jet printing technique. We demonstrate the potential of the developed concept by printing a P3HT interlayer on top of a P3HT-based BHJ with the same solvent system. The approach exploits the in-situ reduction of the aerosol-droplet solvent concentration by high T_{Tube}, reducing the drying time of the DBL from minutes down to seconds. Thereby, the destruction of the underlying layer is prevented and any negative influence on the BHJ's morphology can be avoided successfully. At −2 V reverse bias, OPDs with DBLs printed at $T_{Tube} = 150$ °C show two orders of magnitude lower dark current and a respective reduced S_n compared to the

reference without the DBL. This achieves specific detectivities of about 10^{11} Jones over a range > 4 V reverse bias, fast speeds with a −3 dB cut-off frequency at 864 kHz and a linear dynamic range of 132 dB at 0 V.

We are confident that the introduced printing approach can be extended to many other materials and organic semiconductor devices which otherwise could not be printed due to the limitations from the orthogonal-solvents or cross-linking approach.

4. Experimental Section

Aerosol-Jet Printed Donor Blocking-Layer: All devices were fabricated under cleanroom conditions. 2 g L^{-1} P3HT was diluted in 0.6 mL 1,2-dichlorobenzene mixed with 1,2,4-trichlorobenzene (DCB:TCB) in a ratio of 19:1. TCB was added as a high boiling point solvent to reduce the coffee ring effect. P3HT was printed on top of the annealed BHJ with an Optomec AJ300 aerosol-jet printer. The nozzle size was 150 μm and a serpentine printing pattern was chosen to form squared active areas. The gap between the serpentines was 40 μm, the speed 15 mm s^{-1} and the sheath-gas to aerosol-gas flow ratio 10/21, resulting in a 60 nm layer. The film drying process was observed through the camera of the AJ300 and drying times were recorded with a timer. Devices with DBL printed at $T_{Tube} = 150$ °C were printed first, followed by devices with $T_{Tube} = 20$ °C. The plate temperature was kept constant at 20 °C to ensure a low solubility of the BHJ. The layer was not thermally annealed after deposition to prevent diffusion of the PCBM into the DBL and thereby altering the BHJ morphology.[30,60]

Device Fabrication: Prestructured ITO glass substrates were cleaned mechanically in water and soap as well as with ultrasound in acetone and 2-propanol for 10 min each. Submersion for 5 min oxygen plasma was used as a final cleaning step and surface activation. Zinc oxide (ZnO) nanoparticle solution (N10, Nanograde) was spin-coated at 2000 rpm for 30 s and annealed for 300 s at 120 °C to form a 40 nm HBL. P3HT was mixed with acceptor phenyl-C61-butyric acid methyl ester (PC$_{60}$BM) as a well-known BHJ reference. 40 g L^{-1} P3HT (regio-regular, MW = 58 000, PTL16-08 from Rieke Metals) was stirred in a N2 filled glovebox for >12 h in DCB. 40 g L^{-1} PC$_{60}$BM (Solenne BV). DCB solution was added with a 1:1 ratio. After >1 h stirring, the filtered solution was spin-coated onto the ZnO with 2000 rpm for 30 s followed by 360 s of 300 rpm to form a 60 nm thick layer (or (800 + 300) rpm for (30 + 360) s for a 220 nm thick layer—see Supporting Information). Afterward, the layer was annealed for 10 min at 140 °C in a nitrogen (N$_2$)-atmosphere. On top of the BHJ, the DBL was aerosol-jet printed in cleanroom-air. Devices without this layer served as reference devices. Finally, a 100 nm thick silver (Ag) layer was evaporated as the top electrode and the devices were encapsulated with UV-curable photoresist (Delio Katiobond LP686) and a thin glass slide. The active area was defined by the overlap of the ITO and Ag electrodes leading to a 0.01 cm^2 pixel size (Figure S12, Supporting Information).

Layer Characterization: Pictures of the spin-coated and aerosol-jet printed films were taken with a microscope (Nikon Eclipse 80i) and white light interferometer (Sensofar). Microscopic surface roughness was measured with the AFM (DME Dual-Scope system) and layer

2000811 (6 of 8)

thicknesses and topography (Figure S13, Supporting Information) with a profilometer (Veeco Dektak 150).

Steady-State Characterization: Current–voltage (*IV*) characteristics were measured from −5 to 3 V with a source meter unit (Keithley 2636A). A solar simulator (AM 1.5G; 100 mW cm^{-2}) was used to record illuminated IV curves. We present the best devices however a yield of 95% (in two batches and 64 pixels in total) was achieved and the overall variations are small (see Figure S14 in the Supporting Information for variance). For the LDR a 500 mW laser was used and neutral density filters served to change the intensity (PGL FS-VH, $I_0 = 10$ W cm^{-2}). The spectral responsivities (SR) measurements were performed using a Xenon-discharge lamp (LOT Arc lamp, 450 W Osram XBO) that was filtered to the desired wavelengths by a monochromator (Acton, SP-2150i) and modulated with a chopper-wheel at 173 Hz to serve as a signal. The periodic OPD signals were recorded with a lock-in amplifier (SR830, Stanford Research Systems) after amplification with a trans-impedance amplifier (FEMTO DLPCA-200). The system was calibrated with a silicon photodiode (Thorlabs, FDS100).

Noise Spectral Density and Specific Detectivity: To measure the noise spectral density (S_n), a 20.9 s dark current interval with 90 000 samples was measured with a source meter unit (Keithley A2636), multiplied with the Hann window function and Fourier-transformed into reciprocal space. To avoid the incoupling of pickup-noise, the measurement was conducted in a custom-made shielded metal-box (FEMTO DLPCA-200) directly connected to the box. Moreover, an isolated voltage source (SIM928, SRS) was used to apply different bias voltages via a BNC connection.

The measured SR at 560 nm, the measured frequency-dependent S_n as well as the area A of the OPD were used to calculate the specific detectivity.

Dynamic Characterization: The speed in terms of the OPDs − dB cut-off frequencies was measured by illuminating the OPDs with a periodic optical signal from an Oxxius LBX520 diode laser which was modulated by a square waveform using a function generator (Agilent 33522A). The OPD signal was amplified and recorded with an oscilloscope (Agilent DSO 6102A).

Supporting Information

Supporting Information is available from the Wiley Online Library or from the author.

Conflict of Interest

The authors declare no conflict of interest.

[1] J. Haus, *Optical Sensors: Basics and Applications*, John Wiley & Sons, Hoboken, NJ, USA **2010**.

[2] B. Nabet, *Photodetectors*, Elsevier, Amsterdam, Netherlands **2016**.

[3] I. Yun, *Photodiodes – From Fundamentals to Applications*, InTechOpen, London UK, **2012**.

[4] D. Yang, D. Ma, *Adv. Opt. Mater.* **2019**, *7*, 1800522, https://doi.org/10.1002/adom.201800522.

[5] J. Heikenfeld, A. Jajack, J. Rogers, P. Gutruf, L. Tian, T. Pan, R. Li, M. Khine, J. Kim, J. Wang, J. Kim, *Lab Chip* **2018**, *18*, 217, https://doi.org/10.1039/C7LC00914C.

[6] P. C. Y. Chow, T. Someya, *Adv. Mater.* **2020**, *32*, 1902045, https://doi.org/10.1002/adma.201902045.

[7] S. Cai, X. Xu, W. Yang, J. Chen, X. Fang, *Adv. Mater.* **2019**, *31*, 1808138, https://doi.org/10.1002/adma.201808138.

[8] N. Strobel, M. Seiberlich, R. Eckstein, U. Lemmer, G. Hernandez-Sosa, *Flexible Printed Electron.* **2019**, *4*, 043001, https://doi.org/10.1088/2058-8585/ab56dd.

[9] K.-J. Baeg, M. Binda, D. Natali, M. Caironi, Y.-Y. Noh, *Adv. Mater.* **2013**, *25*, 4267, https://doi.org/10.1002/adma.201204979.

[10] M. Kielar, O. Dhez, G. Pecastaings, A. Curutchet, L. Hirsch, *Sci. Rep.* **2016**, *6*, 39201, https://doi.org/10.1038/srep39201.

[11] N. Strobel, M. Seiberlich, T. Rödlmeier, U. Lemmer, G. Hernandez-Sosa, *ACS Appl. Mater. Interfaces* **2018**, *10*, 42733, https://doi.org/10.1021/acsami.8b16018

[12] N. Gasparini, A. Gregori, M. Salvador, M. Biele, A. Wadsworth, S. Tedde, D. Baran, I. McCulloch, C. J. Brabec, *Adv. Mater. Technol.* **2018**, *3*, 1800104, https://doi.org/10.1002/admt.201800104.

[13] X. Liu, Y. Lin, Y. Liao, J. Wu, Y. Zheng, *J. Mater. Chem. C* **2018**, *6*, 3499, https://doi.org/10.1039/C7TC05042A.

[14] Z. Wu, W. Yao, A. E. London, J. D. Azoulay, T. N. Ng, *Adv. Funct. Mater.* **2018**, *28*, 1800391, https://doi.org/10.1002/adfm.201800391.

[15] R. Eckstein, N. Strobel, T. Rödlmeier, K. Glaser, U. Lemmer, G. Hernandez-Sosa, *Adv. Opt. Mater.* **2018**, *6*, 1701108, https://doi.org/10.1002/adom.201701108.

[16] Y. Khan, D. Han, A. Pierre, J. Ting, X. Wang, C. M. Lochner, G. Bovo, N. Yaacobi-Gross, C. Newsome, R. Wilson, A. C. Arias, *Proc. Natl. Acad. Sci. USA* **2018**, *115*, E11015, https://doi.org/10.1073/pnas.1813053115.

[17] H. Akkerman, B. Peeters, A. van Breemen, S. Shanmugam, D. Tordera, J.-L. van der Steen, A. J. Kronemeijer, P. Malinowski, F. D. Roose, D. Cheyns, J. Genoe, W. Dehaene, P. Heremans, G. Gelinck, *SID Symp. Dig. Tech. Pap.* **2018**, *49*, 494, https://doi.org/10.1002/sdtp.12609.

[18] C. M. Lochner, Y. Khan, A. Pierre, A. C. Arias, *Nat. Commun.* **2014**, *5*, 5745, https://doi.org/10.1038/ncomms6745.

[19] Z. Tang, Z. Ma, A. Sánchez-Díaz, S. Ullbrich, Y. Liu, B. Siegmund, A. Mischok, K. Leo, M. Campoy-Quiles, W. Li, K. Vandewal, *Adv. Mater.* **2017**, *29*, 1702184, https://doi.org/10.1002/adma.201702184.

[20] Z. Liu, K. Parvez, R. Li, R. Dong, X. Feng, K. Müllen, *Adv. Mater.* **2015**, *27*, 669, https://doi.org/10.1002/adma.201403826.

[21] G. Dell'Erba, A. Perinot, A. Grimoldi, D. Natali, M. Caironi, *Semicond. Sci. Technol.* **2015**, *30*, 104005, https://doi.org/10.1088/0268-1242/30/10/104005.

[22] N. Strobel, N. Droseros, W. Köntges, M. Seiberlich, M. Pietsch, S. Schlisske, F. Lindheimer, R. R. Schröder, U. Lemmer, M. Pfannmöller, N. Banerji, G. Hernandez-Sosa, *Adv. Mater.* **2020**, *32*, 1908258, https://doi.org/10.1002/adma.201908258.

[23] D. Cherian, K. Y. Mitra, M. Hartwig, P. E. Malinowski, R. R. Baumann, *IEEE Sens. J.* **2018**, *18*, 94, https://doi.org/10.1109/JSEN.2017.2766700.

[24] N. Strobel, R. Eckstein, J. Lehr, U. Lemmer, G. Hernandez-Sosa, *Adv. Electron. Mater.* **2018**, *4*, 1700345, https://doi.org/10.1002/aelm.201700345.

[25] G. Simone, M. J. Dyson, S. C. J. Meskers, R. A. J. Janssen, G. H. Gelinck, *Adv. Funct. Mater.* **2020**, *30*, 1904205, https://doi.org/10.1002/adfm.201904205.

**ADVANCED
SCIENCE NEWS**

www.advancedsciencenews.com

**ADVANCED
ELECTRONIC
MATERIALS**

www.advelectronicmat.de

[26] R. C. Jones, *Proc. IRE* **1959**, *47*, 1481, https://doi.org/10.1109/JRPROC.1959.287042.

[27] S. Valouch, C. Hönes, S. W. Kettlitz, N. Christ, H. Do, M. F. G. Klein, H. Kalt, A. Colsmann, U. Lemmer, *Org. Electron.* **2012**, *13*, 2727, https://doi.org/10.1016/j.orgel.2012.07.044.

[28] D. Baierl, L. Pancheri, M. Schmidt, D. Stoppa, G.-F. Dalla Betta, G. Scarpa, P. Lugli, *Nat. Commun.* **2012**, *3*, 1175, https://doi.org/10.1038/ncomms2180.

[29] M. Cesarini, B. Brigante, M. Caironi, D. Natali, *ACS Appl. Mater. Interfaces* **2018**, *10*, 32380, https://doi.org/10.1021/acsami.8b07542.

[30] N. D. Treat, M. A. Brady, G. Smith, M. F. Toney, E. J. Kramer, C. J. Hawker, M. L. Chabinyc, *Adv. Energy Mater.* **2011**, *1*, 82, https://doi.org/10.1002/aenm.201000023.

[31] R. Noriega, J. Rivnay, K. Vandewal, F. P. V. Koch, N. Stingelin, P. Smith, M. F. Toney, A. Salleo, *Nat. Mater.* **2013**, *12*, 1038, https://doi.org/10.1038/nmat3722.

[32] S. Stolz, M. Petzoldt, N. Kotadiya, T. Rödlmeier, R. Eckstein, J. Freudenberg, U. H. F. Bunz, U. Lemmer, E. Mankel, M. Hamburger, G. Hernandez-Sosa, *J. Mater. Chem. C* **2016**, *4*, 11150, https://doi.org/10.1039/C6TC04417D.

[33] M. Casutt, M. Ruscello, N. Strobel, S. Koser, U. H. F. Bunz, D. Jänsch, J. Freudenberg, G. Hernandez-Sosa, K. Müllen, *Chem. Mater.* **2019**, *31*, 7657, https://doi.org/10.1021/acs.chemmater.9b02530.

[34] J. Farinhas, Q. Ferreira, R. E. D. Paolo, L. Alcácer, J. Morgado, A. Charas, *J. Mater. Chem.* **2011**, *21*, 12511, https://doi.org/10.1039/C1JM10195A.

[35] K. Peters, S. Raupp, H. Hummel, M. Bruns, P. Scharfer, W. Schabel, *AIP Adv.* **2016**, *6*, 065108, https://doi.org/10.1063/1.4953845.

[36] L. Ahrens, S. Schlisske, K.-P. Strunk, F. Hinkel, C. Melzer, U. H. F. Bunz, U. Lemmer, G. Hernandez-Sosa, D. Jänsch, J. Freudenberg, K. Müllen, *Chem. Mater.* **2018**, *30*, 4157, https://doi.org/10.1021/acs.chemmater.8b01703.

[37] J. Freudenberg, D. Jänsch, F. Hinkel, U. H. F. Bunz, *Chem. Rev.* **2018**, *118*, 5598, https://doi.org/10.1021/acs.chemrev.8b00063.

[38] T. Agostinelli, M. Campoy-Quiles, J. C. Blakesley, R. Speller, D. D. C. Bradley, J. Nelson, *Appl. Phys. Lett.* **2008**, *93*, 203305, https://doi.org/10.1063/1.3028640.

[39] A. Grimoldi, L. Colella, L. La Monaca, G. Azzellino, M. Caironi, C. Bertarelli, D. Natali, M. Sampietro, *Org. Electron.* **2016**, *36*, 29, https://doi.org/10.1016/j.orgel.2016.05.021.

[40] S. Xiong, L. Li, F. Qin, L. Mao, B. Luo, Y. Jiang, Z. Li, J. Huang, Y. Zhou, *ACS Appl. Mater. Interfaces* **2017**, *9*, 9176, https://doi.org/10.1021/acsami.6b16788.

[41] R. Meitzner, T. Faber, S. Alam, A. Amand, R. Roesch, M. Büttner, F. Herrmann-Westendorf, M. Presselt, L. Ciammaruchi, I. Visoly-Fisher, S. Veenstra, A. Diaz de Zerio, X. Xu, E. Wang, C. Müller, P. Troshin, M. D. Hager, S. Köhn, M. Dusza, M. Krassas, S. Züfle, E. Kymakis, E. A. Katz, S. Berson, F. Granek, M. Manceau, F. Brunetti, G. Polino, U. S. Schubert, M. Lira-Cantu, H. Hoppe, *Sol. Energy Mater. Sol. Cells* **2019**, *202*, 110151, https://doi.org/10.1016/j.solmat.2019.110151.

[42] S. Agarwala, G. L. Goh, W. Y. Yeong, *IOP Conf. Ser.: Mater. Sci. Eng.* **2017**, *191*, 012027, https://doi.org/10.1088/1757-899X/191/1/012027.

[43] N. J. Wilkinson, M. A. A. Smith, R. W. Kay, R. A. Harris, *Int. J. Adv. Manuf. Technol.* **2019**, *105*, 4599, https://doi.org/10.1007/s00170-019-03438-2.

[44] Q. Jing, Y. S. Choi, M. Smith, N. Ćatić, C. Ou, S. Kar-Narayan, *Adv. Mater. Technol.* **2019**, *4*, 1800328, https://doi.org/10.1002/admt.201800328.

[45] N. X. Williams, N. Watson, D. Y. Joh, A. Chilkoti, A. D. Franklin, *Biofabrication* **2020**, *12*, 025004, https://doi.org/10.1088/1758-5090/ab5cf5.

[46] F. Machui, S. Langner, X. Zhu, S. Abbott, C. J. Brabec, *Sol. Energy Mater. Sol. Cells* **2012**, *100*, 138, https://doi.org/10.1016/j.solmat.2012.01.005.

[47] C. Montenegro Benavides, S. Rechberger, E. Spiecker, M. Berlinghof, T. Unruh, M. Biele, O. Schmidt, C. J. Brabec, S. F. Tedde, *Org. Electron.* **2018**, *54*, 21, https://doi.org/10.1016/j.orgel.2017.12.022.

[48] F. Z. Dahou, L. Cattin, J. Garnier, J. Ouerfelli, M. Morsli, G. Louarn, A. Bouteville, A. Khelil, J. C. Bernède, *Thin Solid Films* **2010**, *518*, 6117, https://doi.org/10.1016/j.tsf.2010.06.009.

[49] M. Morana, P. Koers, C. Waldauf, M. Koppe, D. Muehlbacher, P. Denk, M. Scharber, D. Waller, C. Brabec, *Adv. Funct. Mater.* **2007**, *17*, 3274, https://doi.org/10.1002/adfm.200700124.

[50] A. Baumann, J. Lorrmann, C. Deibel, V. Dyakonov, *Appl. Phys. Lett.* **2008**, *93*, 252104, https://doi.org/10.1063/1.3055608.

[51] F. Laquai, D. Andrienko, R. Mauer, P. W. M. Blom, *Macromol. Rapid Commun.* **2015**, *36*, 1001, https://doi.org/10.1002/marc.201500047.

[52] S. Trost, T. Becker, A. Polywka, P. Görrn, M. F. Oszajca, N. A. Luechinger, D. Rogalla, M. Weidner, P. Reckers, T. Mayer, T. Riedl, *Adv. Energy Mater.* **2016**, *6*, 1600347, https://doi.org/10.1002/aenm.201600347.

[53] H. F. Haneef, A. M. Zeidell, O. D. Jurchescu, *J. Mater. Chem. C* **2020**, *8*, 759, https://doi.org/10.1039/C9TC05695E.

[54] X. Zhou, D. Yang, D. Ma, A. Vadim, T. Ahamad, S. M. Alshehri, *Adv. Funct. Mater.* **2016**, *26*, 6619, https://doi.org/10.1002/adfm.201601980.

[55] M. R. Esopi, M. Calcagno, Q. Yu, *Adv. Mater. Technol.* **2017**, *2*, 1700025, https://doi.org/10.1002/admt.201700025.

[56] I. K. Kim, J. H. Jo, J. Brian Lee, Y. J. Choi, *Org. Electron.* **2018**, *57*, 89, https://doi.org/10.1016/j.orgel.2018.02.036.

[57] A. van der Ziel, *Proc. IEEE* **1988**, *76*, 233, https://doi.org/10.1109/5.4401.

[58] S. R. Cowan, W. L. Leong, N. Banerji, G. Dennler, A. J. Heeger, *Adv. Funct. Mater.* **2011**, *21*, 3083, https://doi.org/10.1002/adfm.201100514.

[59] A. Pivrikas, N. S. Sariciftci, G. Juška, R. Österbacka, *Prog. Photovoltaics* **2007**, *15*, 677, https://doi.org/10.1002/pip.791.

[60] N. D. Treat, T. E. Mates, C. J. Hawker, E. J. Kramer, M. L. Chabinyc, *Macromolecules* **2013**, *46*, 1002, https://doi.org/10.1021/ma302337p.